Nanoscale Advances

ROYAL SOCIETY OF CHEMISTRY

PAPER

View Article Online
View Journal | View Issue

Cite this: *Nanoscale Adv.*, 2024, **6**, 2075

Boosted photo-immunotherapy *via* near-infrared light excited phototherapy in tumor sites and photo-activation in sentinel lymph nodes†

Chen Wang,[a] Bobo Gu, *[a] Shuhong Qi,*[bc] Siyi Hu *[d] and Yu Wang *[e]

Phototherapy is a promising modality that could eradicate tumor and trigger immune responses *via* immunogenic cell death (ICD) to enhance anti-tumor immunity. However, due to the lack of deep-tissue-excitable phototherapeutic agents and appropriate excitation strategies, the utility of phototherapy for efficient activation of the immune system is challenging. Herein, we report functionalized ICG nanoparticles (NPs) with the capture capability of tumor-associated antigens (TAAs). Under near-infrared (NIR) light excitation, the ICG NPs exhibited high-performance phototherapy, *i.e.*, synergistic photothermal therapy and photodynamic therapy, thereby efficiently eradicating primary solid tumor and inducing ICD and subsequently releasing TAAs. The ICG NPs also captured TAAs and delivered them to sentinel lymph nodes, and then the sentinel lymph nodes were activated with NIR light to trigger efficient T-cell immune responses through activation of dendritic cells with the assistance of ICG NP generated reactive oxygen species, inhibiting residual primary tumor recurrence and controlling distant tumor growth. The strategy of NIR light excited phototherapy in tumor sites and photo-activation in sentinel lymph nodes provides a powerful platform for active immune systems for anti-tumor photo-immunotherapy.

Received 12th January 2024
Accepted 28th February 2024

DOI: 10.1039/d4na00032c

rsc.li/nanoscale-advances

Introduction

Cancer has become one of the major diseases that endanger human health.[1] In addition to the traditional treatment methods of surgical resection, radiotherapy and chemotherapy, various emerging treatment methods have been proposed and demonstrated.[2] Among these newly developed treatment strategies, immunotherapy has revolutionized the treatment of cancer and has achieved remarkable clinical therapeutic effects in various types of cancers.[3] However, it showed ineffectiveness towards solid tumors due to poor immunogenicity, deficiency of antigen presentation and low efficiency of cytotoxic T-lymphocyte infiltration.[4] Moreover, side effects from the possible toxicity of newly developed immunotherapy drugs remarkably hinder the clinical application of immunotherapeutic approaches.[5] Thus, it is imperative to develop a controllable and efficient strategy for enhancing anti-tumor immune response.

Phototherapy, featured with noninvasiveness, low side effects, *etc.*, usually utilizes phototherapeutic agents to selectively kill diseased cells under appropriate light irradiation.[6–12] Light absorbed by phototherapeutic agents is then converted to heat by a photothermal effect in the case of photothermal therapy (PTT) but to reactive oxygen species (ROS) by a photochemical effect in the case of photodynamic therapy (PDT). It has been demonstrated that phototherapy can efficiently lead to immunogenic cell death (ICD) and release of tumor-associated antigens (TAAs) and damaged-associated molecular patterns (DAMPs, *i.e.*, calreticulin (CRT)), increasing the immunogenicity of the tumor microenvironment.[13–15] The exposure of dead cells to TAAs can enhance antigen-specific T-cell responses and the released DAMPs, which can induce dendritic cell (DC) maturation, trigger T-cell activation, and consequently trigger anti-tumor immune response.[16,17] Considering that photo-immunotherapy, with high spatiotemporal precision and excellent safety, has emerged as a promising tool for solid tumor ablation and ICD induction, and therefore various phototherapeutic agents, including aggregation-induced emission luminogens,[18–20] nanosized metal–organic frameworks,[21–23]

[a]*Med-X Research Institute & School of Biomedical Engineering, Shanghai Jiao Tong University, 1954 Huashan Road, Shanghai 200030, China. E-mail: bobogu@sjtu.edu.cn*

[b]*Britton Chance Center for Biomedical Photonics, Wuhan National Laboratory for Optoelectronics, Huazhong University of Science and Technology, Wuhan, Hubei 430074, China*

[c]*MoE Key Laboratory for Biomedical Photonics, School of Engineering Sciences, Huazhong University of Science and Technology, Wuhan, Hubei 430074, China. E-mail: qishuhong@hust.edu.cn*

[d]*CAS Key Laboratory of Bio-Medical Diagnostics, Suzhou Institute of Biomedical Engineering and Technology, Chinese Academy of Sciences, Suzhou 215163, China. E-mail: husiyi@sibet.ac.cn*

[e]*Department of Gynecology, Shanghai First Maternity and Infant Hospital, School of Medicine, Tongji University, Shanghai 200092, China. E-mail: renjiwangyu@126.com*

† Electronic supplementary information (ESI) available. See DOI: https://doi.org/10.1039/d4na00032c

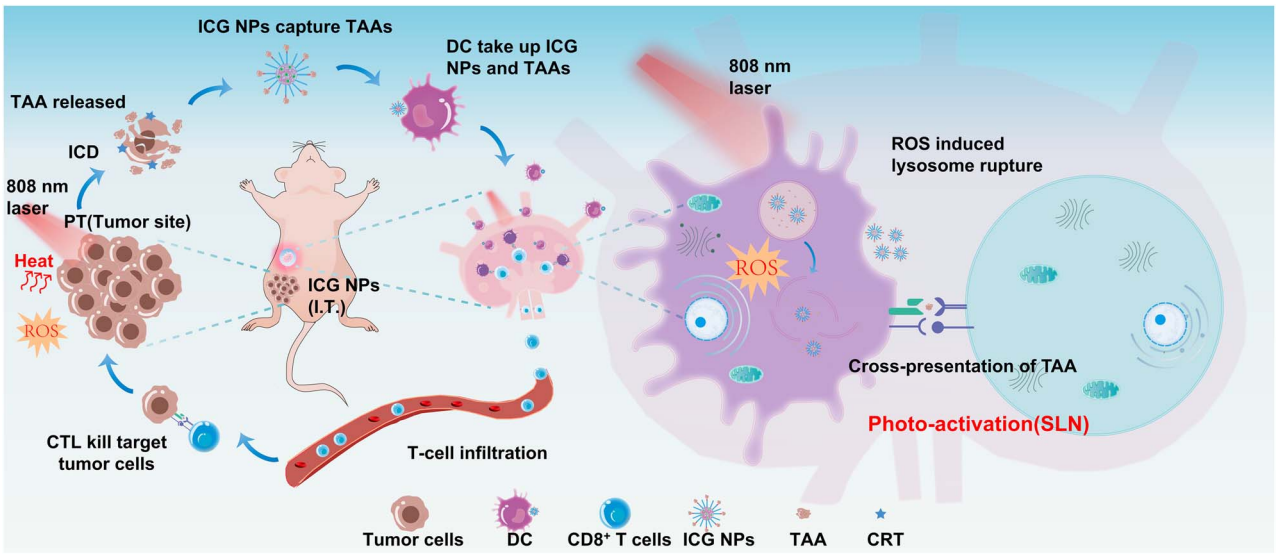

Scheme 1 The mechanism of anti-tumor immune responses triggered by NIR light excited phototherapy and photo-activation. PT: photo-therapy; ICD: immunogenic cell death; TAA: tumor-associated antigens; CRT: calreticulin; DC: dendritic cell; SLN: sentinel lymph node; CTL: cytotoxic lymphocytes; I.T.: intratumoral injection.

black phosphorous (BP) nanomaterial,[24–26] carbon nanomaterial,[27–29] up-conversion nanoparticles,[18,30,31] and subcellular targeted nanoparticles (NPs),[15,32,33] have been designed and synthesized for photo-immunotherapy. However, treating tumors with phototherapy alone is not efficient to induce durable and robust tumor immunogenicity against tumor recurrence and metastasis. For effectively triggering CTL response and cancer photo-immunotherapy, the cross-presentation pathway is a promising method *via* recognition of extracellular antigens on major histocompatibility complex (MHC) class I (MHC-I) molecules in antigen-presenting cells (APC).[34] During this process, the internalized antigen must be transferred from the lysosome to the cytoplasm, and then the transferred antigen is subsequently degraded by the proteasome and presented on MHC-I molecules.[35] The prerequisite for the antigen presenting MHC-I pathway is that foreign antigens could escape from the lysosome and be adequately delivered into the cytoplasm of DCs within the sentinel lymph node.[36] It has been shown that ROS can trigger antigen escape from lysosomes and trigger antigen cross-presentation.[18,37,38] However, due to the lack of deep-tissue-excitable photo-therapeutic agents and appropriate excitation strategies, the utility of phototherapy for immune system activation is challenging, especially in *in vivo* systems.

Here, we designed and synthesized functionalized ICG nanoparticles (NPs) as the phototherapeutic agents to simultaneously induce ICD of tumors and active MHC-I antigen presentation within sentinel lymph nodes under near-infrared (NIR) light excitation for boosted immune responses against primary and distant tumors. The ICG NPs show excellent photothermal effect and ROS generation capability, and the NIR light excited synergistic PTT and PDT could efficiently eradicate the primary solid tumor and induce ICD; moreover, the ICG NPs could capture TAAs and efficiently taken up by APC in the sentinel lymph node. The NIR light irradiation was then performed on sentinel lymph nodes to generate ROS in the DCs, which could induce lysosomal rupture and enable the MHC-I antigen presenting pathway. The significant inhibition of cancer recurrence and systemic metastasis was achieved by the proposed NIR light excitation strategy. The mechanisms of phototherapy-induced immune system activation were also investigated in this study (Scheme 1).

Materials and methods

Materials

Poly(lactic-*co*-glycolic acid (PLGA), Pluronic F68, 1,2-distearoyl-*sn-glycero*-3-phosphoethanolamine-*N*-methoxy (polyethylene glycol)-2000 (DSPE-PEG), 1,2-Distearoyl-*sn-glycero*-3-phosphoethanolamine-*N*-[maleimide(polyethylene glycol)-2000] (DSPE-PEG-MAL), cell counting Kit-8 (CCK-8), 4′,6-diamidino-2-phenylindole (DAPI), 7′-dichlorofluorescin diacetate (DCFH-DA), dimethyl sulfoxide (DMSO), calcein acetoxymethyl ester (calcein-AM), and propidium iodide (PI) were purchased from Sigma-Aldrich. RPMI medium, DMEM medium, and phosphate buffered saline were purchased from HyClone. Fetal calf serum was purchased from ScienCell. Calreticulin Polyclonal Antibody, Goat anti-ChickenIgY(H+L) Cross-Absorbed Secondary Antibody, Alexa Fluor 633- conjugated secondary antibody, anti-PE-CD11c, anti-FITC-CD80, anti-APC-CD86, and Pieroe BCA protein assay kit were purchased from ThermoFisher. Ovalbumin was purchased from Macklin. 1,3-Diphenyl isobenzofuran (DPBF) was purchased from Aladdin. Indocyanine Green (ICG) was purchased from Absin.

Synthesis of ICG NPs

6 mg PLGA was dissolved in 3 mL acetonitrile to form an organic solution. ICG (0.6 mg), Pluronic F68 (15 mg), DSPE-PEG

(15 mg) and DSPE-PEG-MAL (0.5 mg) were dissolved in 3 mL ultrapure water to form an aqueous solution mixture. Then, the organic solution and aqueous solution mixture were injected into 24 mL ultrapure water using a syringe pump (PHD Ultra, Harvard Apparatus, USA), which was followed by the ultrasound treatment for 5 min (130 W, 20 kHz). Finally, the ICG NPs were filtered three times using an Amicon ultra-4 centrifugal filter (5500 rpm, 25 °C, 10 min) and then were obtained for the following studies.

Characterization of ICG NPs

The hydrodynamic sizes and zeta potential of ICG NPs were measured using Zetasizer Nano ZSP. The absorption and fluorescence spectra were recorded with a spectrophotometer (UV1901PC) and fluorescence spectrometer (FLS1000), respectively.

The encapsulation efficiency of ICG loaded in NPs was determined as follows: the standard concentration–absorption curve was measured by the different concentrations of free ICG using a microplate reader (SpectraMax i3x, MOLECULAR DEVICES). The absorption of synthesized ICG NPs was measured and compared with the standard concentration–absorption curve to determine their concentration. The loading efficiency was calculated by the concentration of ICG NPs and raw ICG.

Singlet oxygen measurements

In order to measure the ROS generation capability of synthesized ICG NPs, DPBF was selected as the ROS indicator. 100 μL of DPBF solution (0.5 mg mL^{-1}) was separately added to 3 mL of DI water, 3 mL of ICG solution (10 μg mL^{-1}), and 3 mL of ICG NPs solution (10 μg mL^{-1}), which was followed by light irradiation (808 nm, 1 W cm^{-2}). The time-sequenced absorbance of the solution mixture at 420 nm was recorded to evaluate the ROS generation capability of ICG.

Antigen capture capability

After encapsulation with DSPE-PEG or DSPE-PEG-MAL, 5 mg of the formed UCNPs-DSPE-PEG/UCNPs-DSPE-PEG-MAL was separately mixed with 2.5 mg of OVA, which was stirred for 24 h. The solution mixture was centrifuged at 3000 rpm for 10 min to obtain OVA@UCNPs-DSPE-PEG/OVA@UCNPs-DSPE-PEG-MAL, and the supernatant was collected to measure the concentration of OVA using a bicinchoninic acid (BCA) assay, enabling the quantification and comparison of the antigen capture capability of UCNPs-DSPE-PEG/UCNPs-DSPE-PEG-MAL.

Cell culture

4T1 cells were cultured in the RPMI 1640 medium containing 10% fetal calf serum (FBS), 1% penicillin and streptomycin at 37 °C in a humidified atmosphere containing 5% CO_2.

Fluorescence imaging of ICG NPs-treated cells

4T1 cells were seeded in confocal dishes at a density of 2×10^5 cells and incubated for 24 h in a humidified atmosphere containing 5% CO_2. The cells were washed with PBS three times and then treated with ICG NPs (50 μg mL^{-1}). After 6 h of co-incubation, the 4T1 cells were washed with PBS to remove the residual ICG NPs, which was followed by fluorescence imaging using a homemade NIR-II wide-field imaging system.

Cytotoxicity test

4T1 cells were seeded in 96-well plates (1×10^4 cells per well, 100 μL per well). Once the cells adhered to the wall and the density was appropriate, various concentrations of ICG NPs were added and incubated for 24 h. After washing with a fresh medium to remove the residual nanocomposite, the treated cells were incubated with CCK-8, which was dissolved in RPMI 1640 medium. After 1.5 h of incubation, the absorption at 450 nm was measured by the microplate reader (SpectraMax i3x, MOLECULAR DEVICES).

To measure the cell viability under light irradiation conditions, 4T1 cells were seeded in 96-well plates (1×10^4 cells per well, 100 μL per well). Once the cells adhered to the wall and the density was appropriate, various concentrations of ICG NPs were added and incubated for 6 h, and then laser irradiation (808 nm, 1 W cm^{-2}) was performed for 10 min. After incubation for 3 h, the light-treated cells were washed with a fresh medium to remove the residual ICG NPs and subsequently incubated with CCK-8 for another 1.5 h, which was dissolved in the RPMI/1640 medium. Finally, the absorption at 450 nm was measured by a microplate reader (SpectraMax i3x, MOLECULAR DEVICES). The cell viability was calculated by the following formula:

$$\text{Cell viability } (\%) = \frac{OD - OD_{blank}}{OD_{control} - OD_{blank}} \times 100$$

Intracellular ROS generation capability of ICG NPs

In order to visualize the intracellular ROS generation capability of ICG NPs, ICG NPs were incubated with 4T1 cells (50 μg mL^{-1}) for 6 h. After being replaced with fresh RPMI 1640 medium (without FBS) containing 10 mM DCFH-DA, the 4T1 cells were further incubated for 30 min. After the incubation, the cells were washed 3 times with fresh RPMI medium to remove the redundant DCFH-DA and irradiated with 808 nm laser for 30 s or 60 s. The treated cells were imaged using confocal laser scanning microscopy to evaluate the intracellular ROS generation.

In vitro phototherapy

After being incubated with ICG NPs (50 μg mL^{-1}) or culture medium of RPMI for 6 h, the 4T1 cells were irradiated with 808 nm laser (1 W cm^{-2}, 10 min or 0 min) and subsequently incubated in a fresh medium for 3 h, which was followed by incubating with calcein-AM (2 μM) and PI (2 μM) for 30 min. After washing three times with PBS, the treated cells were imaged using confocal laser scanning microscopy to evaluate the *in vitro* phototherapy effect.

Detection of CRT

The 4T1 cells were incubated with ICG NPs (50 μg mL^{-1}) for 12 h, washed with PBS, and treated with light irradiation (808 nm, 1 W cm^{-2}) for 10 min, which was followed by another 12 h incubation. Thereafter, the cells were washed with PBS and fixed with 4% paraformaldehyde for 20 min. The fixed cells were incubated with anti-calreticulin antibody (1 : 200 dilution) for 12 h at 4 °C and stained with Alexa Fluor 633-conjugated secondary antibody (1 : 200 dilution) for 2 h at room temperature. The ecto-CRT and expressions of cells were detected using confocal laser scanning microscopy.

Acquisition of murine bone marrow-derived dendritic cells (BMDCs)

BALB/c mice (6 weeks of age) were sacrificed, all femurs and tibias were removed, and the surrounding muscle tissues were removed as cleanly as possible. The extracted bones were soaked in a sterile Petri dish containing 70% alcohol for 3 min to disinfect and sterilize and then washed twice with sterile PBS. The bone, both ends cut off with scissors, was moved into another new Petri dish containing PBS, and PBS was extracted with a syringe. The needle was inserted into the bone marrow cavity from both ends of the bone, and the bone marrow was repeatedly rinsed out into the Petri dish until the bone was completely white. Bone marrow suspension was collected, and a 70 μm cell strainer was used to remove small debris and muscle tissue. The collected filtrate was centrifuged at 1200 rpm for 5 min to remove the supernatant. 2 mL ammonium chloride red cell lysate was added into the cell collection solution, and the cells were suspended and incubated at room temperature for 3 min. 10 mL PBS was added to neutralize the lysate, and then the cell collection solution was centrifuged at 1200 rpm for 5 min, and the supernatant was discarded. Mouse bone marrow cells were obtained by washing with PBS once and then re-suspending with RPMI 1640 medium containing 10% FBS. The obtained mouse bone marrow cells were counted and adjusted to 1×10^6 mL^{-1} with RPMI 1640 medium containing 10% FBS. 4 mL of RPMI 1640 complete medium, which contained 10% FBS and supplemented with GM-CSF (20 ng mL^{-1}) and IL-4 (10 ng mL^{-1}), was used to culture BMDCs in 6-well plates with a cell density of 1×10^6 cells per mL. On days 2 and 4, the culture medium was gently replaced with the fresh medium mentioned above. On day 6, immature BMDCs were harvested for further experiments.

In vitro detection of BMDC maturation

As described before, BMDCs were extracted from femurs and tibias of BALB/c mice (6 weeks old). On day 6, immature BMDCs were counted and seeded into the lower chamber of the Transwell (2×10^5 cells per well). 4T1 tumor cells were counted and seeded at the upper chamber (1×10^5 cells per well).

Different groups were treated differently. These transwells were randomly divided into five groups, including the control group (without any treatment), light group (4T1 cells were irradiated with an 808 nm laser (1 W cm^{-2}, 10 min) in the upper layer, the BMDCs in the lower layer are not treated) phototherapy group (after incubation with ICG NPs (50 μg mL^{-1}) for 6 h, the 4T1 cells were irradiated with 808 nm laser (1 W cm^{-2}, 10 min) in the upper layer, the BMDCs in the lower layer are not treated) and phototherapy combined with the photo-activation group (after incubation with ICG NPs (50 μg mL^{-1}) for 6 h, the 4T1 cells were irradiated with 808 nm laser (1 W cm^{-2}, 10 min) in the upper layer, after the 4T1 cells and BMDCs were co-incubated for 4 h or 6 h, respectively, the BMDCs were photo-activated with 808 nm laser (0.2 W cm^{-2}, 60 min and avoid light for 30 seconds every five minutes during the irradiation) in the lower layer). After 24 h incubation, the BMDCs were washed and stained with antibodies, including anti-PE-CD11c, anti-FITC-CD80, and anti-APC-CD86. Finally, all the samples were re-suspended in a flow buffer (1% FBS in PBS) before being analyzed by flow cytometry. All the flow cytometric analysis was conducted using the FACSAria II (BD Biosciences), and data analysis was carried out using FlowJo software (**http://www.flowjo.com**; Tree Star).

Animal models

All animal procedures were performed in accordance with the Guidelines for Care and Use of Laboratory Animals of Shanghai Jiao Tong University and approved by the Animal Ethics Committee of the School of Biomedical Engineering, Shanghai Jiao Tong University. BALB/c mice (6 weeks old) were purchased from JSJ. The breast tumor model was established by subcutaneous injection of 4T1 cells (1×10^6 cells in 100 μL per mouse) into the right second row of breast pads to obtain the primary tumor. On the same day, 4T1 cells (2×10^5 cells in 50 μL per mouse) were subcutaneously injected into the same back from the distant tumor. Once the primary tumor volume reached about 80 mm^3, hair on the back of mice was removed by depilatory cream prior to the *in vivo* experiments.

In vivo imaging and biodistribution analysis

BALB/c mice (6 weeks old) were randomly divided into two groups, with 3 mice in each group. The mice in each group were injected with 0.15 mg kg^{-1} of either free ICG or ICG NPs. Fluorescence images and semi-quantitative analysis of ICG were performed at 0, 6, 12, 24 and 48 h after injection with the *ex*/*in vivo* imaging system (IVIS Spectrum). The mice were sacrificed at 48 h after injection, and the major organs, including heart, liver, spleen, lung, kidneys and tumor were collected for imaging and semi-quantitative analysis.

In vivo sentinel lymph node imaging

Before performing the *in vivo* imaging, the position of sentinel lymph nodes corresponding to the right second nipple of mice was coarsely localized using methylene blue. Then, 10 μL ICG NPs solutions (10 μg mL^{-1}) were injected subcutaneously near the nipple of 4T1 tumor-bearing mice, and the corresponding sentinel lymph nodes of mice were imaged using a homemade NIR-II optical imaging system at different time points.

In vivo phototherapy

The phototherapy was performed when the primary tumor volume reached about 80 mm^3. The tumor-bearing mice were randomly divided into five groups, including the control group (without any treatment), ICG NPs group (intratumoral injection of 0.15 mg kg^{-1} ICG NPs), light group (irradiation with light (808 nm, 1 W cm^{-2}, 10 min)), phototherapy group (intratumoral injection of 0.15 mg kg^{-1} ICG NPs and irradiation with light (808 nm, 1 W cm^{-2}, 10 min)) and phototherapy combined with photo-activation group (intratumoral injection of 0.15 mg kg^{-1} ICG NPs and irradiation with light (808 nm, 1 W cm^{-2}, 10 min)) at the primary tumor and the low-power photo-activation at the sentinel lymph node was performed 6 h after primary tumor treatment, the sentinel lymph node was irradiated (808 nm, 0.2 W cm^{-2}, 60 min and avoid light for 30 s every five minutes during the irradiation) on day 0 and day 1. After these treatments, the tumor sizes were measured with a vernier caliper and calculated using the formula:

$$\text{Tumor volume} = \frac{\text{length} \times \text{width} \times \text{width}}{2}$$

The tumor growth inhibition rates (IR) were calculated *via* the following formula:

$$\text{IR } (\%) = \left(1 - \frac{TV_t}{TV_c}\right) \times 100$$

where TV_t represents the mean tumor volume of the treated groups and TV_c represents the mean tumor volume of the control group.

Statistical analysis

Data are reported as mean ± SEM. The differences among groups were determined using unpaired *T*-test analysis: $^*P < 0.05$, $^{**}P < 0.01$, $^{***}P < 0.001$.

Results

Characterization of ICG NPs

Indocyanine green (ICG) is the only FDA (Food and Drug Administration) approved near infra-red (NIR) contrast agent[39] and possesses a high absorption efficiency in the NIR region, making it an excellent phototherapeutic agent, but it suffers from unstable optical properties, quick degradation, clearance in the living body, *etc.* In order to improve the intravital phototherapeutical outcomes *via* its enhanced penetration and retention (EPR) effect, ICG was encapsulated with an amphiphilic polymer to form ICG nanoparticles (NPs). ICG NPs were self-assembled using a solution mixture of ICG, PLGA, DSPE-PEG, Pluronic F68 *via* the sonication method (Fig. 1A and Fig. S1†). PLGA encapsulated the ICG to form the core, which was followed by DSPE-PEG self-assemblies around the PLGA core to form a single layer of lipid to stabilize the core. Pluronic F68 surfactant was also added to further enhance the stability. The self-assembled ICG NPs had a uniform diameter of around 69 nm with a polydispersity of 0.108 (Fig. 1B), which could endow ICG NPs with the passive tumor targeting capability due to the EPR effect. The zeta potential of ICG NPs, which has a very intimate relation to the stability of the suspension,[40] was measured as −37.1 mV, indicating the good stability of the synthesized ICG NPs. Due to the F68 surfactant, the ICG NPs showed excellent photostability within 4 weeks (Fig. S2†), enabling long-term *in vivo* applications. The formed ICG NPs exhibited a broad absorption band from 500 to 900 nm with a peak at 784 nm and an emission peak at 825 nm (Fig. 1C), which was similar to that of the free ICG molecule, indicating that the encapsulation had no significant influence on the optical features of ICG. Meanwhile, the encapsulation efficiency, one key parameter to estimate the synthesis method, was calculated to be 33.4% by measuring and comparing the absorption of free ICG and ICG NPs (Fig. S3†). The photothermal effect of ICG and ICG NPs was monitored and compared using an infrared (IR) thermal imaging camera (Fig. 1D and E). Under laser irradiation (808 nm, 1 W cm^{-2}) for 3 min, the temperature of ICG NPs solution rose from 26.2 °C to 61.7 °C, which could induce irreversible damage to tumor cells, while that of ICG solution only rose to 55.4 °C. Meanwhile, the temperature of water was almost kept constant, eliminating any interference from water absorption. It indicated that ICG NPs had much better photothermal efficiency than free ICG, making it a good agent for photothermal therapy (PTT). The remarkably enhanced photothermal effect could be ascribed to encapsulation-induced local high concentration of ICG and less dissipation pathway of heat.

In addition to the photothermal effect, the photochemical effect, *i.e.*, reactive oxygen species (ROS) generation capability, was also investigated using DPBF as an indicator (Fig. 1F and G). Under laser irradiation (808 nm, 1 W cm^{-2}), DPBF was efficiently decomposed in the presence of ICG or ICG NPs, but the decomposition of DPBF in the presence of ICG NPs was much faster than that in the presence of free ICG (Fig. 1H), indicating that encapsulation could also enhance the ROS generation capability. Recent studies have shown that ROS levels in cancer cells above the toxic threshold can overwhelm the antioxidant system and induce cell death, thus regulating the immunogenicity of dying cancer cells.[41,42] In addition, ROS can achieve cytoplasmic antigen delivery by promoting antigen escape from lysosomes in dendritic cells, thereby improving the efficiency of antigen cross-presentation and subsequent effective T-cell priming and expansion.[18,37,38] The good ROS production capability makes ICG NPs have the potential to be an immune stimulant.

To realize the active capture of TAAs, DSPE-PEG-MAL was used to encapsulate ICG, making the surface of formed ICG NPs rich in the MAL group. Considering the MAL group could bind to proteins by forming stable thioether bonds,[43] the formed ICG NPs could have the capability to improve the photoimmunotherapeutic outcomes *via* the active capture of TAAs. To verify the capture capability of the MAL group, DSPE-PEG and DSPE-PEG-MAL were used to encapsulate up-conversion nanoparticles (UCNPs), which had a much larger mass than ICG NPs and facilitated subsequent separation, to form UCNPs-DSPE-PEG and UCNPs-DSPE-PEG-MAL, respectively. UCNPs-

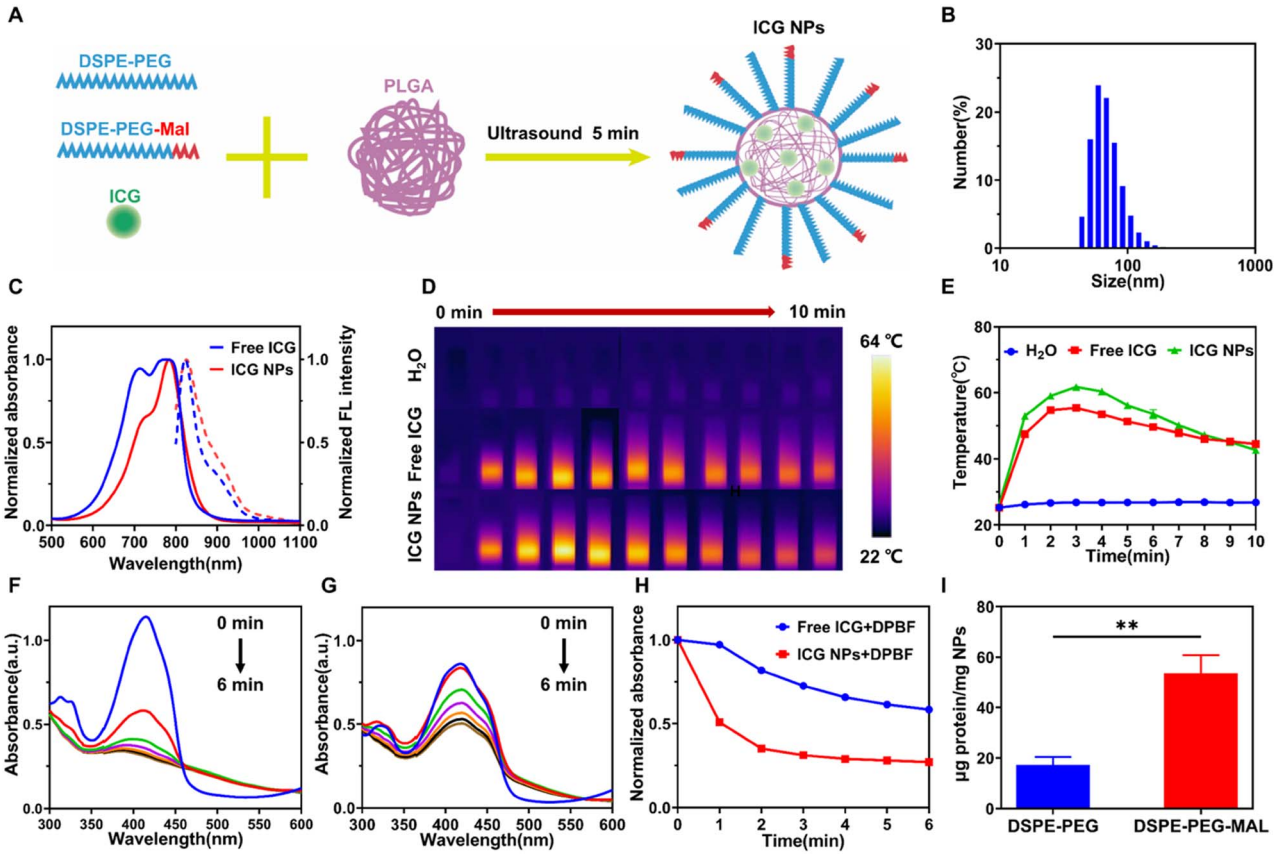

Fig. 1 Preparation and characterization of ICG NPs. (A) Schematic illustration of ICG nanoparticle synthesis process. (B) The hydrodynamic size distribution of ICG NPs. (C) Normalized absorption (solid lines) and emission (dashed lines) spectra of ICG NPs. [ICG] = 10 μg mL^{-1}. (D) Infrared thermographic maps and (E) temperature variations of H_2O, free ICG and ICG NPs under laser irradiation. [ICG] = 30 μg mL^{-1}, light irradiation (800 nm, 1 W cm^{-2}). Absorption spectra variations of DPBF incubated with (F) ICG NPs or (G) free ICG under laser irradiation for different times. [ICG] = 10 μg mL^{-1}, [DPBF] = 16 μg mL^{-1}, light irradiation (800 nm, 1 W cm^{-2}). (H) Absorption variation of different solution mixtures at 420 nm with the increment of irradiation time. (I) Quantification of OVA captured by UCNPs modified with DSPE-PEG or DSPE-PEG-MAL.

DSPE-PEG and UCNPS-DSPE-PEG-MAL were separately mixed with standard antigen model ovalbumin (OVA) and centrifuged to separate the free OVA, and then the capture capability of UCNPs-DSPE-PEG and UCNPs-DSPE-PEG-MAL was evaluated (Fig. 1I). It showed that the MAL group could efficiently capture OVA, indicating that DSPE-PEG-MAL encapsulated ICG NPs could actively capture TAAs.

In vitro phototherapy

Before performing the *in vitro* and *in vivo* phototherapy, the biocompatibility and cellular uptake capability of ICG NPs were evaluated. 4T1 cells were incubated with ICG NPs of various concentrations for 24 h, and then the CCK-8 kit assay was used to assess the cell viability (Fig. S4†). There was no significant difference between the control cells and ICG NPs treated cells, indicating the excellent biocompatibility of ICG NPs. Thereafter, 4T1 cells were incubated with ICG NPs on confocal dishes; the NIR fluorescence imaging showed that ICG NPs could efficiently light up cells with a high signal-background ratio (Fig. S5†), indicating the good cellular uptake rate of ICG NPs. The excellent biocompatibility and cellular uptake capability ensured its biomedical applications.

It has been demonstrated that ROS could induce lysosomal rupture to facilitate the cytosolic release of antigen and subsequently cross-presentation.[18] Therefore, the intracellular ROS generation capability of ICG NPs was studied. 2′,7′-Dichlorofluorescin-diacetate (DCFH-DA), which could be rapidly oxidized in the presence of ROS to yield the highly fluorescent signal of dichlorofluorescein (DCF), was selected as the ROS indicator. After incubating either with both ICG NPs and DCFH-DA or with DCFH-DA alone, the treated 4T1 cells were irradiated with different power and imaged with confocal laser scanning microscopy (Fig. 2A). In the initial scans, strong fluorescence of DCF was observed, and seemed to reach a plateau when the scan times reached 60 s for the high-power irradiation (808 nm, 1 W cm^{-2}). Meanwhile, the apparent fluorescence of DCF was also observed even in the low-power irradiation (808 nm, 0.2 W cm^{-2}). It demonstrated the effective and rapid intracellular ROS generation capability of ICG NPs. In contrast, there was no fluorescent signal in the absence of ICG NPs, eliminating the possibility of any laser-induced interference with the obtained results.

Considering that the ICG NPs possessed good photothermal effects and intracellular ROS generation capability, the

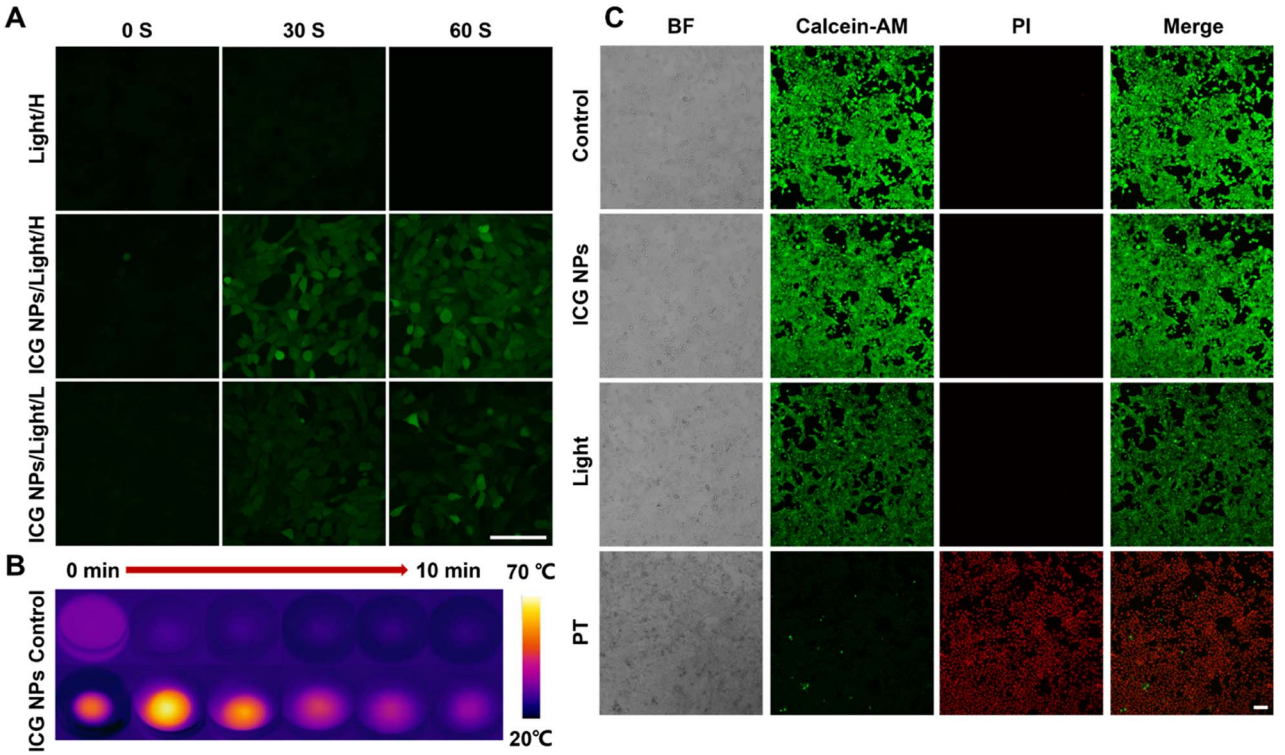

Fig. 2 Characterization of *in vitro* phototherapeutical outcomes. (A) Study of the intracellular ROS generation capability of ICG NPs under different irradiation power (H: high power intensity, 1 W cm^{-2}, L: low power intensity, 0.2 W cm^{-2}). [ICG] = 50 μg mL^{-1}, [DCFH-DA] = 5 μM, DCF channel (Ex: 488 nm, Em: 500–550 nm), scale bar: 100 μm. (B) Time-sequenced infrared thermographic maps of 4T1 cells incubated with/out ICG NPs under laser irradiation (808 nm, 1 W cm^{-2}). [ICG] = 50 μg mL^{-1}. (C) Optical images of calcein-AM (green) and PI (red) co-stained 4T1 cells treated with nothing (control), ICG NPs, light irradiation (light), and both with ICG NPs and light irradiation (PT). Light irradiation: 808 nm, 1 W cm^{-2}. Calcein-AM channel (Ex: 488 nm; Em: 505–525 nm) and PI channel (Ex: 552 nm; Em: 605–625 nm), [calcein-AM] = 2 μM, [PI] = 2 μM, scale bar: 100 μm.

synergistic phototherapy of PTT and PDT was investigated *via in vitro* cancer cell ablation effect. The 4T1 cells were incubated with different concentrations of ICG NPs for 6 h and then treated with laser irradiation (808 nm, 1 W cm^{-2}) for 10 minutes, which was followed by cell viability evaluation using CCK-8 kit assay. The IC_{50} values for ICG were measured as 15.18 μg mL^{-1} (Fig. S6†). In order to further study the therapeutic effect of ICG NPs based phototherapy, the treated 4T1 cells were stained with calcein-acetoxymethyl ester (calcein-AM) and propidium iodide (PI) for viability analysis using confocal laser scanning microscopy (Fig. 2C). All cells treated with both ICG NPs and light irradiation, *i.e.*, phototherapy group, were PI-positive since PI is a fluorescent nucleic acid stain that can permeate only the damaged membranes, it can be deduced that membranes of the nucleus were damaged by phototherapy, demonstrating the good anti-tumor activity. During the phototherapy process, the temperature changes of the treated/untreated cells were recorded with an infrared thermal imager (Fig. 2B). It showed that the temperature of ICG NPs treated cells could rise up to 68 °C, indicating the excellent PTT effect. Meanwhile, the temperature of untreated cells was almost kept constant (Fig. S7†), eliminating the possibility of any laser-induced thermal effect on the obtained results. It has been demonstrated that PDT and PTT can give full play to the advantages of each treatment and make up for the limitations of the other.[44] Thus, ICG NPs based synergistic phototherapy could achieve superior therapeutic outcomes.

ICD induction and immune cell activation by ICG NPs *in vitro*

It has been demonstrated that the phototherapy could induce dying tumor cells to release DAMPs such as CRT *via* ICD, activating the immune response.[45] To verify its capability to induce ICD in tumor cells, ICG NPs were incubated with 4T1 cells, which was followed by phototherapy with high-power light irradiation (808 nm, 1 W cm^{-2}) for 10 min. It was observed that ICG NPs based phototherapy induced obvious surface-exposed CRT (Fig. 3A), while there was no CRT signal in the control and light groups, eliminating any interference from light irradiation. This result indicated that the high-power laser excited phototherapy could efficiently induce ICD and the release of DAMPs from 4T1 tumor cells, which could provide potential antigenic stimulation for anti-tumor immune response.

The immune activation effect of ICG NPs based photoactivation to bone marrow dendritic cells (BMDCs) was subsequently investigated (Fig. 3B). 4T1 cells and BMDCs were cultured in the upper and lower layers of the transwell for 24 h, respectively. The 4T1 cells were treated with both ICG NPs and high-power light irradiation (*i.e.*, PT group), high-power light

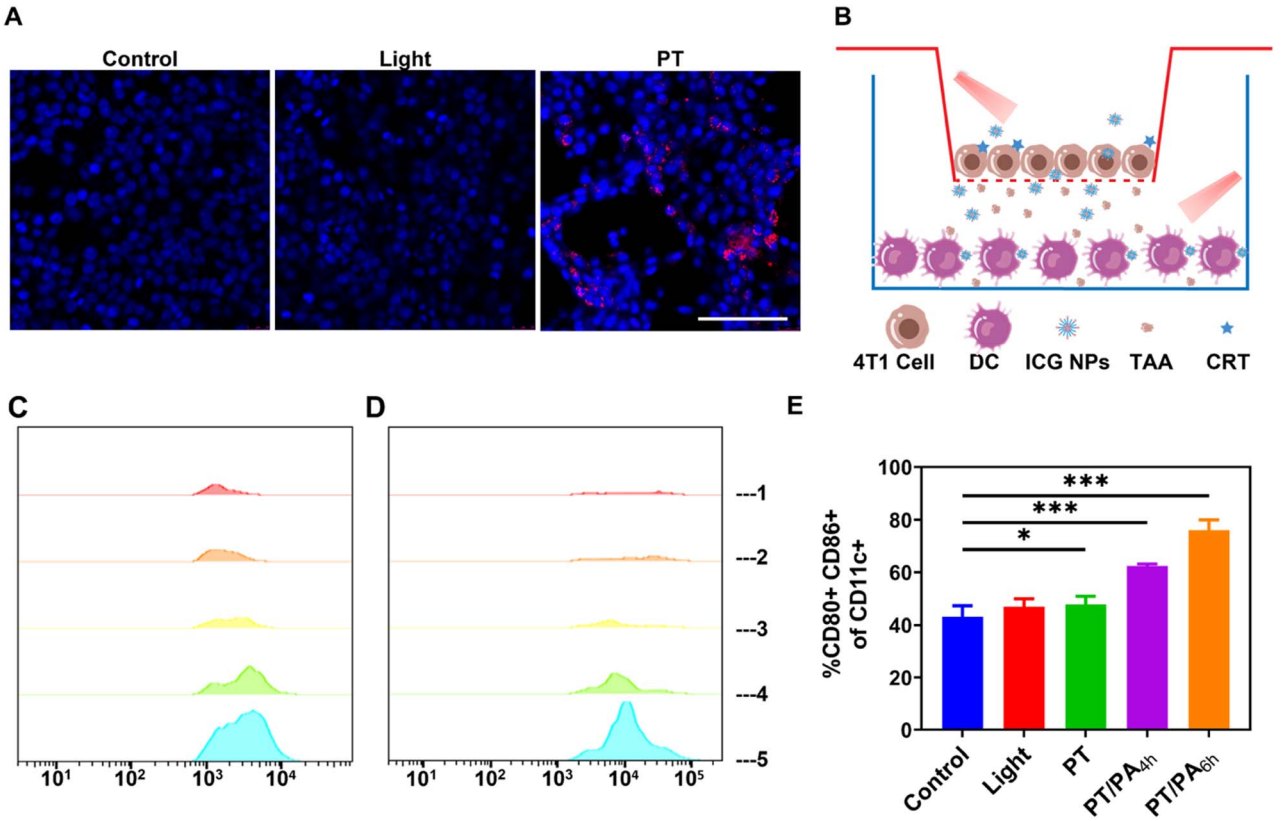

Fig. 3 ICD induction and immune cell activation by ICG NPs *in vitro*. (A) Fluorescent imaging of ecto-CRT expression of 4T1 cells treated with nothing (control), light irradiation (light), and both light irradiation and ICG NPs (PT). Light irradiation: 808 nm, 1 W cm^{-2}, 10 min. [ICG] = 50 μg mL^{-1}. DAPI channel (Ex: 405 nm, Em: 415–485 nm). CRT channel (Ex: 633 nm, Em: 640–670 nm). Scale bar: 100 μm. (B) Schematic illustration of the detection methods of BMDC maturation *in vitro*. FACS analysis of (C) $CD80^+$ and (D) $CD86^+$ expression on BMDCs under low-power NIR irradiation (gated on $CD11c^+$). (1) Control; (2) light; (3) PT; (4) PT/PA_{4h}; (5) PT/PA_{6h}. (E) Quantitative analysis of the mean fluorescence intensity (MFI) of BMDCs co-expressing $CD80^+$ and $CD86^+$ after different treatments ($n = 3$). Statistical significance was assessed using unpaired *T*-test analysis. Data are represented as means ± SEM. $^*P < 0.05$, and $^{***}P < 0.001$.

irradiation (*i.e.*, light group), and nothing (*i.e.*, control group), respectively. After the treatment in the upper layer, the whole transwell was incubated for 6 h. Finally, the BMDCs were collected for flow cytometry analysis. It was observed that BMDCs in light and control groups exhibited very weak CD80 and CD86 expression, while the CD80 and CD86 expression was increased in the PT group (Fig. 3C and D). It indicated that the phototherapy could promote the maturation of dendritic cells and thus activate the immune effect. To further enhance the immune activation effect, low-power photo-activation (808 nm, 0.2 W cm^{-2}, 60 min) was performed on the BMDCs in the lower layer, which was co-cultured with phototherapy treated 4T1 cells in the upper layer for 4 h or 6 h (*i.e.*, PT/PA_{4h} or PT/PA_{6h} groups). The flow cytometer results showed that the photo-activation could efficiently increase CD80 and CD86 expression (Fig. 3C and D). In order to further characterize the maturation and activation of DC, the proportion of CD80 and CD86 double-positive cells in dendritic cells was measured (Fig. 3E and S8†). The results showed that photo-activation induced more mature dendritic cells, which co-expressed CD80 and CD86. The proportion of CD80 and CD86 double positive dendritic cells in the PT/PA group was about 76.1% (PT/PA_{6h}) and 62.5% (PT/PA_{4h}), compared with 43.1% in the control group. The enhanced immune activation effect could be ascribed to the low-power light irradiation generated ROS-induced lysosomal rupture, which facilitated the cytosolic release of antigen and subsequently cross-presentation. It was worth noting that PT/PA_{6h} has higher CD80 and CD86 expression than PT/PA_{4h}. It means that properly prolonging the incubation time can enhance the interaction between BMDCs with DAMPs and TAA generated by dying 4T1 tumor cells, and consequently the maturation of BMDCs.

In vivo and *ex vivo* biodistribution of ICG and ICG NPs

Before performing the *in vivo* photo-immunotherapy, the *in vivo* and *ex vivo* fluorescence images were acquired at various time intervals to study the biodistribution of the administrated ICG and ICG NPs (Fig. 4A and B). Once intratumoral injection of ICG or ICG NPs, strong fluorescence was observed in the tumor site. With an increment of time, the fluoresce signal in the tumor site gradually weakened, which was attributed to the diffusion of ICG or ICG NPs. Due to the EPR effect, the decrement rate of the fluorescence signal of ICG NPs was smaller than that of ICG. It indicated that ICG NPs could efficiently reach the whole tumor

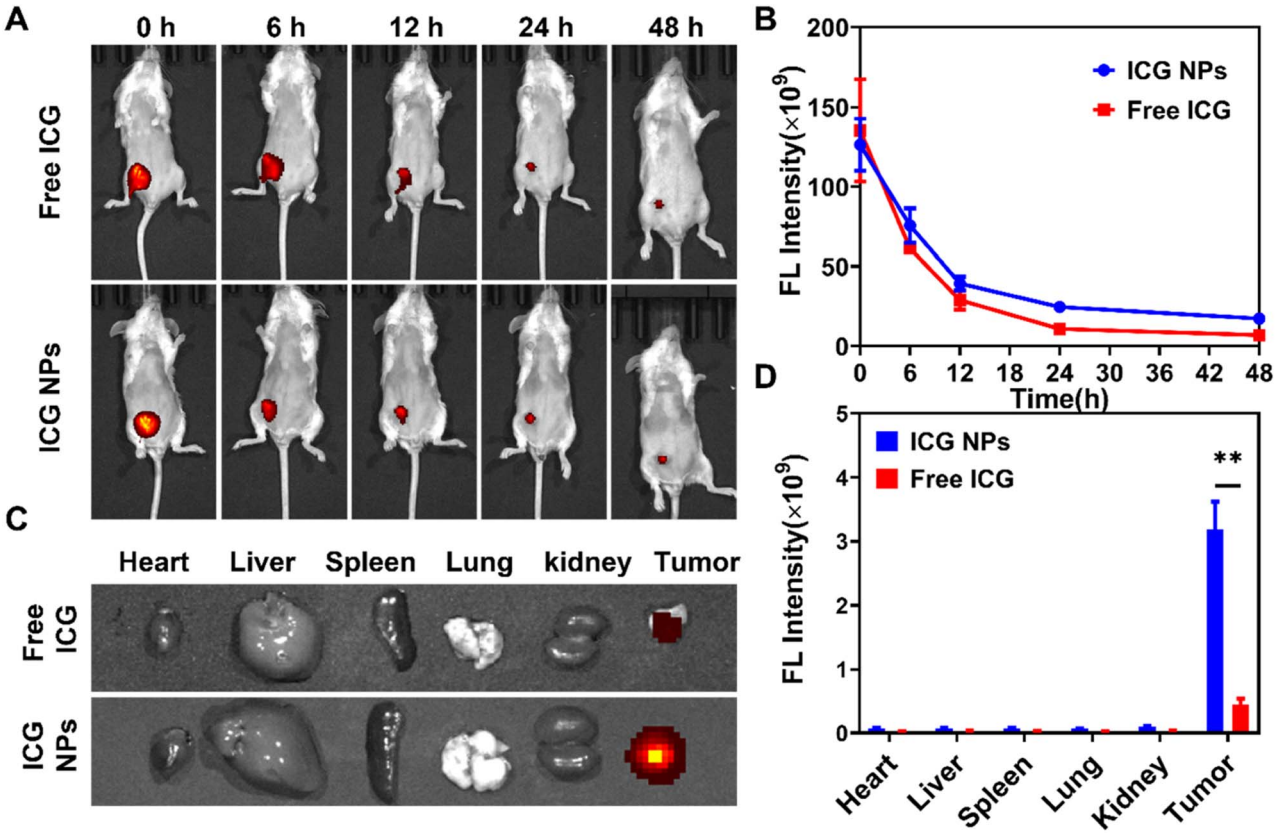

Fig. 4 Biodistribution of free ICG and ICG NPs. (A) Time-sequenced *in vivo* fluorescence images of free ICG (0.15 mg kg^{-1}) and ICG NPs (0.15 mg kg^{-1}) treated mice. (B) Normalized fluorescence intensity in tumor sites at different times post-injection of free ICG and ICG NPs ($n = 3$). (C) *Ex vivo* fluorescence images of tumors and major organs at 48 h post-injection of free ICG and ICG NPs. (D) Normalized fluorescence intensity in tumor and major organs at 48 h post-injection of free ICG and ICG NPs ($n = 3$). Data are represented as means ± SEM. $^{**}P < 0.01$.

with a longer retention time. The fluorescent images of major organs and tumors excised from mice at 48 h post intratumoral injection of ICG or ICG NPs were also captured for analysis (Fig. 4C and D), and the ICG NPs treated tumor showed much stronger fluorescence signal than other organs, which was consistent with the *in vivo* fluorescence images. All these results demonstrated the effective preferential accumulation of ICG NPs in tumors.

In vivo photo-immunotherapy performance

The synthesized ICG NPs have shown excellent immune activation capability and *in vitro* phototherapy outcomes, making ICG NPs a promising *in vivo* photo-immunotherapy agent. The orthotopic breast cancer model was established by inoculating 4T1 cells in the abdominal mammary fat pad as the primary tumor. Considering that ICG NPs could capture the antigen, the NIR-II fluorescence imaging method was performed to study whether the intratumorally injected ICG NPs would reach sentinel lymph nodes. After locating the sentinel lymph nodes with methylene blue (Fig. 5B), the tumor was stained *via* intratumoral injection of ICG NPs, which was followed by sentinel lymph node imaging using an InGaAs camera at different time points (Fig. 5C). It was observed that the ICG NPs would reach sentinel lymph nodes 2 h after intratumoral injection and remained within sentinel lymph nodes for several hours, enabling the stimulation of dendritic cells in sentinel lymph nodes and consequently enhance immune activation effect by low-power photo-activation.

In order to investigate the photo-immunotherapeutic outcomes by NIR light excited phototherapy, the distant tumor was subcutaneously planted on the dorsal side of the same side (Fig. 5A). After intratumoral injection of ICG NPs (0.15 mg kg^{-1}) in the primary tumor, mice were immediately irradiated with high-power light irradiation on the primary tumor site (808 nm, 1W cm^{-2}) for 10 min for the PT group or 0 min for the PS group, respectively, while the mice in the control and light groups were only treated with PBS or light irradiation, respectively. Moreover, the temperature during the treatment was monitored by an IR thermal camera. The treatment temperature could reach 50 °C, ensuring efficient phototherapy (Fig. 5D and S9A†). Then, on day 0 and day 1 after phototherapy of the primary tumor, low power photoactivation (808 nm, 0.2 W cm^{-2}, 60 min with 0.5 min interval every 5 min to eliminate the photothermal effect) was performed on sentinel lymph nodes for immune activation under the guidance of NIR-II imaging (*i.e.*, PT/PA group). The IR thermal camera also monitored the temperature of sentinel lymph nodes, and no significant temperature rise was observed, indicating the negligible photothermal effect on immune cell

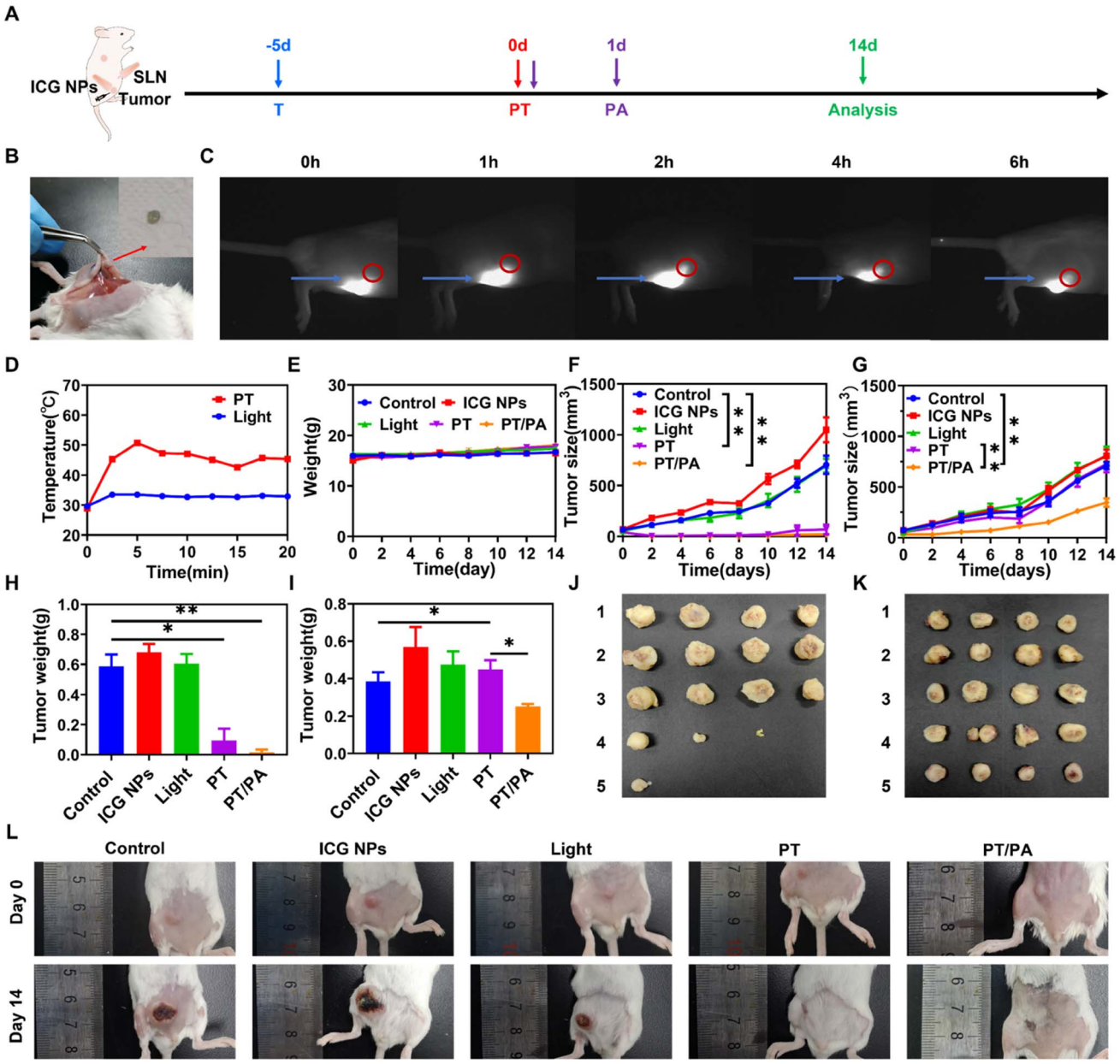

Fig. 5 *In vivo* photo-immunotherapy performance. (A) Schematic illustration of the synergistic treatment schedule. T: tumor inoculation; PT: phototherapy; PA: photo-activation of sentinel lymph node stimulation. (B) Sentinel lymph node (marked by the red arrow) tracing with methylene blue. (C) Sentinel lymph node imaging *via* NIR-II imaging method at different times after ICG NPs injection. Excitation: 808 nm, 10 mW cm^{-2}. The blue arrows indicated the tumors, and the red circles indicated the sentinel lymph nodes. (D) Body weights of 4T1 tumor mice treated with different treatments ($n = 4$). (E) Temperature variation during phototherapy. (F) The primary tumor and (G) the distant tumor growth curves of the 4T1 tumor-bearing mice with different treatments ($n = 4$). (H) The primary tumor and (I) the distant tumor weight of the 4T1 tumor-bearing mice with different treatments ($n = 4$). (J) The photo of the primary tumor and (K) the distant tumor of the 4T1 tumor-bearing mice with different treatments ($n = 4$). (1) control; (2) ICG NPs; (3) light; (4) PT; (5) PT/PA. (L) The photo of the 4T1 tumor-bearing mice with different treatments on day 0 and day 14. Data represent means ± SEM. *$P < 0.05$, **$P < 0.01$.

activation (Fig. S9B and C†). After treatment and photo-activation, the mice weights and tumor sizes of both primary and distant tumors were measured every 2 days. There was no significant body weight loss for all groups within 2 weeks, as shown in Fig. 5E. It was obvious that the size of the primary tumor in the control, light and PS groups kept increasing quickly, while the primary tumor size of PT and PT/PA groups was significantly decreased after phototherapy treatment (Fig. 5F). Two weeks after the treatment, the primary tumor suppression rates were 97.4% and 90% in the PT/TA and PT groups, respectively. Meanwhile, the distant tumor size of the control, light, PS and PT groups still kept increasing, but the distant tumor size increment rate of PT/PA was much lower than that of other groups (Fig. 5G). At the end of the treatment, the PT group had no obvious inhibition effect on the distant tumor, while the PT/PA group had an inhibition rate of 51.4%,

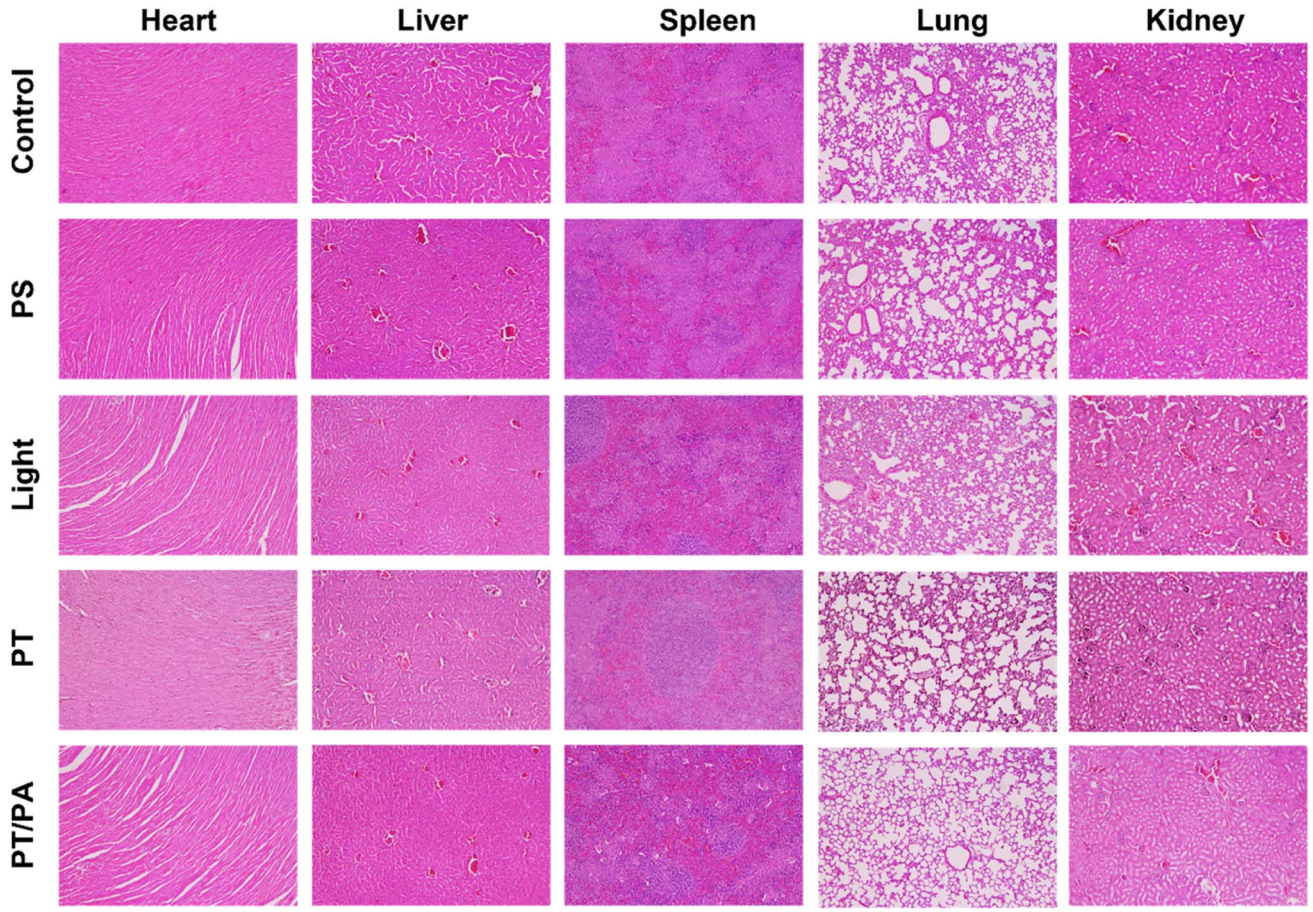

Fig. 6 H&E images of the major organs collected from healthy and treated mice at day 14. Scale bar: 200 μm.

indicating the efficient immune response activation endowed by photo-activation in sentinel lymph nodes. It was worth noting that the primary tumor size of the PT/PA group was not increased within 14 days and was much smaller than that of the PT group, indicating that the photo-activation enhanced immune response efficiently inhibited residual primary tumor recurrence.

All mice were sacrificed on day 14, and the practical tumor weight and tumor morphology are shown in Fig. 5H-L. The primary tumors of PT and PT/PA groups were significantly reduced, even completely disappeared, confirming the effectiveness of the ICG NPs based phototherapy. Among all the distant tumors, the PT/PA group had the smallest volume, confirming the efficient immune response activation. Meanwhile, the major organs, including the heart, kidney, liver, lung, and spleen, were also collected from sacrificed mice, which were treated with PS, PT, PT/PA, *etc.*, for analysis *via* H&E staining. As shown in Fig. 6, there were no signs of organ lesions for all groups, confirming the excellent *in vivo* biocompatibility of ICG NPs.

Conclusions

We proposed a new photo-immunostimulant design based on ICG NPs to achieve effective immune response *via* high-performance phototherapy in the tumor site and photo-activation at the sentinel lymph node. The synthesized ICG NPs with superior biocompatibility not only avoid the possible side effect of newly developed phototherapeutical agents but also actively capture released TAAs to promote an immune response. Photothermal and photochemical effects have been demonstrated to cause ICD of tumor cells and release TAAs. Meanwhile, ROS have also been regarded as efficient signal molecules for improving the efficiency of antigen cross-presentation and subsequent effective T-cell priming and expansion. Under NIR light irradiation, the phototherapy integrating PTT and PDT could efficiently ablate primary solid tumors and induce ICD. The ICG NPs could capture TAAs and be drained to the sentinel lymph node, which was observed using the NIR-II imaging method. After optimizing the time interval by observing the NIR-II fluorescence signal, photo-activation was performed under the guidance of NIR-II imaging on sentinel lymph nodes to generate ROS to regulate the activation of DCs and enhance cross-presentation of antigen. The NIR light excited photo-activation on DCs induced a stronger immune response than that without additional irradiation, which was demonstrated using flow cytometry analysis. The phototherapy induced immune response not only inhibited residual primary tumor recurrence but also controlled distant tumor growth. The excellent photo-immunotherapeutic

outcomes could be ascribed to (I) phototherapeutic agents were excited by NIR light that has a much larger penetration depth as compared with visible light, enabling efficient phototherapy in tumor site and photo-activation in sentinel lymph nodes; (II) the prepared ICG NPs could capture TAAs and be drained to sentinel lymph nodes, and with low-power photo-activation in the sentinel lymph node, ROS was generated to trigger efficient T-cell immune responses *via* MHC-I antigens presentation.

In summary, we developed a versatile phototherapeutical agent, ICG NPs, for boosting photo-immuno-therapeutical outcomes. The phototherapy on the tumor site eradicated the solid tumor and released TAAs *via* ICD, while the photo-activation on the sentinel lymph node triggered an efficient immune response, reducing the risk of cancer recurrence and metastasis. Due to the superior biocompatibility of ICG NPs and the induced excellent photo-immunotherapeutic outcomes, the proposed cancer treatment possesses great potential for future translational research.

Author contributions

B. Gu and C. Wang conceived the idea. B. Gu and C. Wang designed the research. C. Wang performed the experiments. C. Wang, B. Gu, S. Qi, S. Hu and Y. Wang analyzed the data. B. Gu and C. Wang wrote and revised the manuscript, and all authors reviewed the manuscript.

Conflicts of interest

All authors declare that they have no conflict of interest or financial conflicts to disclose.

Acknowledgements

This work was supported by the National Key Research and Development Program of China (2021YFF0502900), the National Natural Science Foundation of China (62375169), Shanghai Jiao Tong University (YG2022ZD005, YG2024QNA06).

References

1 R. L. Siegel, K. D. Miller, N. S. Wagle and A. Jemal, *Ca-Cancer J. Clin.*, 2023, **73**, 17–48.
2 J. Zugazagoitia, C. Guedes, S. Ponce, I. Ferrer, S. Molina-Pinelo and L. Paz-Ares, *Clin. Ther.*, 2016, **38**, 1551–1566.
3 K. Esfahani, L. Roudaia, N. Buhlaiga, S. V. Del Rincon, N. Papneja and W. H. Miller, *Curr. Oncol.*, 2020, **27**, S87–S97.
4 J. P. Bates, R. Derakhshandeh, L. Jones and T. J. Webb, *BMC Cancer*, 2018, **18**, 87–97.
5 M. A. Postow, R. Sidlow and M. D. Hellmann, *N. Engl. J. Med.*, 2018, **378**, 158–168.
6 V. N. Nguyen, Z. Zhao, B. Z. Tang and J. Yoon, *Chem. Soc. Rev.*, 2022, **51**, 3324–3340.
7 H. Y. Shi and P. J. Sadler, *Br. J. Cancer*, 2020, **123**, 871–873.
8 L. Y. Lin, W. Pang, X. Y. Jiang, S. H. Ding, X. B. Wei and B. B. Gu, *Light: Sci. Appl.*, 2022, **11**, 47.
9 W. Pang, Z. Y. Xiao, X. B. Wei and B. B. Gu, *Opt. Lett.*, 2023, **48**, 3849–3852.
10 S. H. Ding, W. B. Wu, T. T. Peng, W. Pang, P. F. Jiang, Q. Q. Zhan, S. H. Qi, X. B. Wei, B. B. Gu and B. Liu, *Nanoscale Adv.*, 2021, **3**, 2325–2333.
11 W. Pang, P. F. Jiang, S. H. Ding, Z. Z. Bao, N. T. Wang, H. X. Wang, J. L. Qu, D. Wang, B. B. Gu and X. B. Wei, *Adv. Healthcare Mater.*, 2020, **9**, 2000607.
12 B. B. Gu, W. B. Wu, G. X. Xu, G. X. Feng, F. Yin, P. H. J. Chong, J. L. Qu, K. T. Yong and B. Liu, *Adv. Mater.*, 2017, **29**, 1701076.
13 X. P. Duan, C. Chan and W. B. Lin, *Angew. Chem., Int. Ed.*, 2019, **58**, 670–680.
14 W. J. Yang, F. W. Zhang, H. Z. Deng, L. S. Lin, S. Wang, F. Kang, G. C. Yu, J. Lau, R. Tian, M. R. Zhang, Z. T. Wang, L. C. He, Y. Ma, G. Niu, S. Hu and X. Y. Chen, *ACS Nano*, 2020, **14**, 620–631.
15 H. Z. Deng, Z. J. Zhou, W. J. Yang, L. S. Lin, S. Wang, G. Niu, J. B. Song and X. Y. Chen, *Nano Lett.*, 2020, **20**, 1928–1933.
16 J. Nam, S. Son, K. S. Park, W. P. Zou, L. D. Shea and J. J. Moon, *Nat. Rev. Mater.*, 2019, **4**, 398–414.
17 L. Galluzzi, I. Vitale, S. Warren, S. Adjemian, P. Agostinis, A. Buqué Martinez, T. A. Chan, G. Coukos, S. Demaria, E. Deutsch, D. Draganov, R. L. Edelson, S. C. Formenti, J. Fucikova, L. Gabriele, U. S. Gaipl, S. R. Gameiro, A. D. Garg, E. Golden, J. Han, K. J. Harrington, A. Hemminki, J. W. Hodge, D. M. S. Hossain, T. Illidge, M. Karin, H. L. Kaufman, O. Kepp, G. Kroemer, J. J. Lasarte, S. Loi, M. T. Lotze, G. Manic, T. Merghoub, A. A. Melcher, K. L. Mossman, F. Prosper, O. Rekdal, M. Rescigno, C. Riganti, A. Sistigu, M. J. Smyth, R. Spisek, J. Stagg, B. E. Strauss, D. L. Tang, K. Tatsuno, S. W. van Gool, P. Vandenabeele, T. Yamazaki, D. Zamarin, L. Zitvogel, A. Cesano and F. M. Marincola, *J Immunother Cancer*, 2020, **8**, e000337.
18 D. Mao, F. Hu, Z. G. Yi, K. Kenry, S. D. Xu, S. Q. Yan, Z. C. Luo, W. B. Wu, Z. H. Wang, D. L. Kong, X. G. Liu and B. Liu, *Sci. Adv.*, 2020, **6**, eabb2712.
19 Z. Y. Liu, J. T. Zhang, H. Liu, H. L. Shen, N. H. Meng, X. W. Qi, K. Ding, J. Song, R. Fu, D. Ding and G. X. Feng, *Adv. Mater.*, 2023, **35**, 2208692.
20 C. Chen, X. Ni, S. R. Jia, Y. Liang, X. L. Wu, D. L. Kong and D. Ding, *Adv. Mater.*, 2019, **31**, 1904914.
21 G. X. Lan, K. Y. Ni, Z. W. Xu, S. S. Veroneau, Y. Song and W. B. Lin, *J. Am. Chem. Soc.*, 2018, **140**, 5670–5673.
22 Z. X. Cai, F. L. Xin, Z. W. Wei, M. Wu, X. Y. Lin, X. F. Du, G. Chen, D. Zhang, Z. X. Zhang, X. L. Liu and C. P. Yao, *Adv. Healthcare Mater.*, 2020, **9**, 1900996.
23 Q. X. Wang, Y. F. Yang, X. F. Yang, Y. Pan, L. D. Sun, W. Y. Zhang, Y. L. Shao, J. Shen, J. Lin, L. L. Li and C. H. Yan, *Nano Today*, 2022, **43**, 101439.
24 Z. J. Xie, M. H. Peng, R. T. Lu, X. Y. Meng, W. Y. Liang, Z. J. Li, M. Qiu, B. Zhang, G. H. Nie, N. Xie, H. Zhang and P. N. Prasad, *Light: Sci. Appl.*, 2020, **9**, 161.
25 X. G. Zhang, J. J. Tang, C. Li, Y. Lu, L. L. Cheng and J. Liu, *Bioact. Mater.*, 2021, **6**, 472–489.

26 D. Y. Xu, J. Liu, Y. X. Wang, Y. Y. Jian, W. W. Wu and R. C. Lv, *ACS Biomater. Sci. Eng.*, 2020, **6**, 4940–4948.
27 M. Zhang, W. T. Wang, F. Wu, T. Zheng, J. Ashley, M. Mohammadniaei, Q. C. Zhang, M. Q. Wang, L. Li, J. Shen and Y. Sun, *Biomaterials*, 2020, **252**, 120106.
28 H. He, Z. Y. Fei, T. L. Guo, Y. Hou, D. Li, K. F. Wang, F. Z. Ren, K. L. Fan, D. J. Zhou, C. M. Xie, C. Wang and X. Lu, *Biomaterials*, 2022, **280**, 121272.
29 L. J. Luo, C. Liu, T. He, L. Y. Zeng, J. Xing, Y. Z. Xia, Y. W. Pan, C. Y. Gong and A. G. Wu, *Nanoscale*, 2018, **10**, 22035–22043.
30 H. Yu, Q. Wang, X. M. Zhang, A. Tiemuer, J. Wang, Y. Y. Zhang, X. L. Sun and Y. Liu, *Biomater. Sci.*, 2023, **11**, 2167–2176.
31 J. Xu, L. G. Xu, C. Y. Wang, R. Yang, Q. Zhuang, X. Han, Z. L. Dong, W. W. Zhu, R. Peng and Z. Liu, *ACS Nano*, 2017, **11**, 4463–4474.
32 C. Zhang, F. Gao, W. Wu, W. X. Qiu, L. Zhang, R. Q. Li, Z. N. Zhuang, W. Y. Yu, H. Cheng and X. Z. Zhang, *ACS Nano*, 2019, **13**, 11249–11262.
33 Y. H. Li, X. Zhang, X. Y. Wan, X. H. Liu, W. Pan, N. Li and B. Tang, *Adv. Funct. Mater.*, 2020, **30**, 2000532.
34 A. R. Sánchez-Paulete, A. Teijeira, F. J. Cueto, S. Garasa, J. L. Pérez-Gracia, A. Sánchez-Arráez, D. Sancho and I. Melero, *Ann. Oncol.*, 2017, **28**, 44–55.
35 K. L. Yang, A. Halima and T. A. Chan, *Nat. Rev. Clin. Oncol.*, 2023, **20**, 604–623.
36 M. Embgenbroich and S. Burgdorf, *Front. Immunol.*, 2018, **9**, 1643.
37 O. J. Norum, P. K. Selbo, A. Weyergang, K. E. Giercksky and K. Berg, *J. Photochem. Photobiol., B*, 2009, **96**, 83–92.
38 C. Wang, P. Li, L. L. Liu, H. Pan, H. C. Li, L. T. Cai and Y. F. Ma, *Biomaterials*, 2016, **79**, 88–100.
39 I. J. Fox and E. H. Wood, *Proc. Staff Meet. Mayo Clin.*, 1960, **35**, 732–744.
40 S. Kamble, S. Agrawal, S. Cherumukkil, V. Sharma, R. V. Jasra and P. Munshi, *Chemistryselect*, 2022, **7**, e202103084.
41 B. Li, G. Y. Hao, B. Sun, Z. Gu and Z. P. Xu, *Adv. Funct. Mater.*, 2020, **30**, 1909745.
42 B. W. Yang, Y. Chen and J. L. Shi, *Chem. Rev.*, 2019, **119**, 4881–4985.
43 Y. Z. Min, K. C. Roche, S. M. Tian, M. J. Eblan, K. P. McKinnon, J. M. Caster, S. J. Chai, L. E. Herring, L. Z. Zhang, T. Zhang, J. M. DeSimone, J. E. Tepper, B. G. Vincent, J. S. Serody and A. Z. Wang, *Nat. Nanotechnol.*, 2017, **12**, 877–882.
44 Z. J. Xie, T. J. Fan, J. An, W. Choi, Y. H. Duo, Y. Q. Ge, B. Zhang, G. H. Nie, N. Xie, T. T. Zheng, Y. Chen, H. Zhang and J. S. Kim, *Chem. Soc. Rev.*, 2020, **49**, 8065–8087.
45 J. H. Zou, L. Li, Z. Yang and X. Y. Chen, *Nanophotonics*, 2021, **10**, 3229–3245.